Nano Research 2018, 11(1): 195–205
https://doi.org/10.1007/s12274-017-1619-y
Research Article
ISSN 1998-0124
CN 11-5974/O4

Layered double hydroxide monolayers for controlled loading and targeted delivery of anticancer drugs

Xuan Mei, Simin Xu, Tongyang Hu, Liuqi Peng, Rui Gao, Ruizheng Liang (✉), Min Wei (✉), David G. Evans, and Xue Duan

State Key Laboratory of Chemical Resource Engineering, Beijing Advanced Innovation Center for Soft Matter Science and Engineering, Beijing University of Chemical Technology, Beijing 100029, China

Received: 10 November 2016
Revised: 9 April 2017
Accepted: 11 April 2017

KEYWORDS
two-dimensional,
nanomaterials,
monolayer,
layered double hydroxide (LDH),
drug loading,
controllable release

ABSTRACT

Two-dimensional (2D) nanomaterials have gained tremendous attention in the field of biomedicine because of their high specific surface areas and fascinating physicochemical properties. Herein, 2D monolayered double hydroxide (MLDH) nanosheets were employed to localize doxorubicin (DOX), an anticancer drug, with a loading capacity of as high as 3.6 mg·mg^{-1} (*w*/*w*). Structural characterizations and theoretical calculations indicate that the DOX molecule is uniformly arranged and oriented at the surface of the MLDHs with a binding energy of 15.90 eV, showing significant electrostatic interaction. With the assistance of the targeting agent folic acid (FA), DOX-FA/MLDHs demonstrate targeted cellular uptake and superior anticancer behavior based on *in vitro* tests performed with cancer cells. In addition, this composite material exhibits a selective release toward cancer cells and good biocompatibility with normal cells, which would guarantee its practical applications in cancer therapy.

1 Introduction

Recently, two-dimensional (2D) nanomaterials such as transition metal dichalcogenides (TMDs), graphene, and black phosphorus have drawn considerable attention in the field of biomedicine area on account of their high specific surface areas and unique chemical and physical properties [1–6]. In virtue of their remarkable surface area to mass ratio, highly efficient drug loading can be achieved with atomically thin 2D structures [7–11]. For instance, graphene has been widely explored as cancer therapy carriers, biosensing platforms, and disease diagnosis agents [12–14]. Moreover, the 2D TMD nanomaterial MoS_2 has been applied in photothermal therapy while black phosphorus was used as a photodynamic agent [15, 16]. Although some fascinating developments based on 2D nanomaterials have been made [17–21], they are still far from satisfaction for utilization in biomedicine, especially as drugs carriers. The main problem is

Address correspondence to Ruizheng Liang, liangruizheng2000@163.com; Min Wei, weimin@mail.buct.edu.cn

ungratified targeting, unselective drug release, and weak biocompatibility. Moreover, control over particle size and complicated synthesis urgently need to be improved. Therefore, the fabrication of 2D nanocomposites with targeted and selective release as well as superior biocompatibility remains a challenge.

As a class of 2D nanomaterials, the structure of layered double hydroxides (LDHs) can be represented by the general formula $[M^{2+}_{1-x}M^{3+}_{x}(OH)_2](A^{n-})_{x/n}\cdot mH_2O$, where M^{2+} and M^{3+} are divalent and trivalent cations and A^{n-} acts as the charge-balancing and exchangeable interlayer anion [22–26]. By virtue of this unique structure, LDHs have been widely explored as inorganic composite materials for drug/gene delivery, demonstrating controllable drug release and excellent biocompatibility [27–31]. Compared with bulk LDHs, monolayer LDH (MLDH) nanosheets exhibit much higher specific surface and more combinative sites, leading to greatly enhanced surface activity for drug loading. Moreover, because of the ultra-thin structure and basic property of MLDHs, promoted drug release performance could be obtained in the intercellular environments of cancer cells (pH = 5.5, slight acidic) as opposed to normal cells (pH = 7.4) [32–35]. Therefore, the incorporation of MLDHs and pharmaceutical drugs could result in improved loading and selective release, enhancing the anticancer performance and reducing side effects to normal cells.

Herein, we develop MLDH nanosheets as a drug carrier for cellular imaging and chemotherapy. MLDH nanosheets were synthesized through a facile delamination process, followed by incorporation with the chemotherapeutic agent doxorubicin (DOX), which showed extremely high loading efficiency and controllable release behavior. Moreover, folic acid (FA) was introduced to improve the targeting ability toward cancer cells (Scheme 1). X-ray diffraction, atomic force microscopy, and high-resolution transmission electron microscopy demonstrated the successful preparation of the MLDH nanosheets with a diameter of ~ 50 nm and a thickness of ~ 0.8 nm. Ultraviolet visible (UV-vis) spectroscopy and Fourier transform infrared spectroscopy confirmed the loading of DOX with a capacity of 3.6 $mg\cdot mg^{-1}$ (*w*/*w*), which is significantly higher than the reported values so far [36–38]. *In vitro* tests performed with KB cancer cells

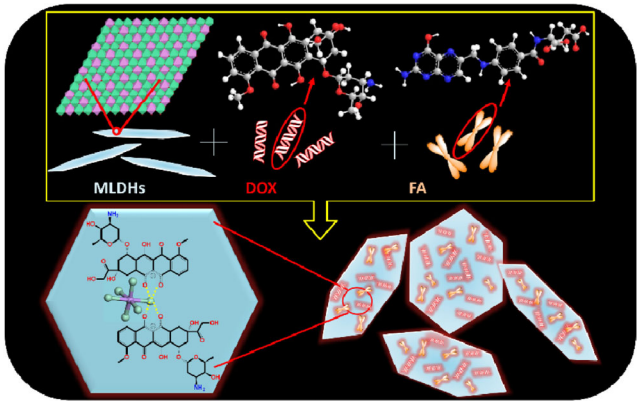

Scheme 1 Schematic representation of the fabrication process of FA-DOX/MLDHs.

demonstrated targeted cellular uptake, imaging, and superior anticancer performance of FA-DOX/MLDHs. In addition, this composite material displays selective release toward cancer cells and good biocompatibility with normal cells, which would guarantee its further applications in cancer therapy.

2 Experimental

2.1 Materials

Doxorubicin, folic acid, and 7-ethyl-10-hydroxy-camptothecin (SN38) were purchased from Sigma-Aldrich, China. $Mg(NO_3)_2\cdot 6H_2O$, $Al(NO_3)_3\cdot 9H_2O$, NaOH, $NaNO_3$, graphite, NaCl, $KMnO_4$, H_2O_2, formamide, N-(3-dimethylaminopropyl-N′-ethylcarbodiimide hydrochloride) (EDC), and 2-arm polyetheylene glycol-amine were purchased from Aladdin Chemical. Co. Ltd, China. The chemicals were all of analytical grade and used without purification. deionized water was used in all experimental processes.

2.2 Synthesis of LDH monolayer nanosheets

MgAl-LDH monolayer nanosheets were synthesized via a method reported previously [39], but with some modifications. Typically, solution A was composed of $Mg(NO_3)_2\cdot 6H_2O$ (0.0008 mol) and $Al(NO_3)_3\cdot 9H_2O$ (0.0002 mol) dissolved in 20 mL of deionized water. Solution B was composed of NaOH (0.005 mol) dissolved in 20 mL of deionized water. Solution C was composed of $NaNO_3$ (0.0002 mol) dissolved in a mixed solvent containing 15 mL of deionized water and 5 mL

of formamide. Solution A and solution B were added dropwise into solution C with stirring at 90 ˚C for 20 min, and the resulting precipitation was centrifuged three times with deionized water. A dialysis (8 kDa) treatment was performed to remove the residual formamide to obtain the final LDH monolayer nanosheets.

2.3 Synthesis of PEGylated graphene oxide

A modified Hummer's method was used to synthesize graphene oxide (GO) [40]. Graphite (1.0 g) and NaCl (50.0 g) were ground thoroughly for 10 min, followed by washing with water to remove NaCl. The graphite flakes were stirred in H_2SO_4 (23 mL, 98%) for 12 h. Afterwards, $KMnO_4$ (6.0 g) was added and heated up to 105 ˚C for 25 min followed by dripping a H_2O_2 solution (10 mL, 30%). After washing the resulting product, a NaOH solution (10 mL, 120 mg·mL^{-1}) was added to the GO suspension (10 mL, ~ 4 mg·mL^{-1}) and bath-sonicated for 4 h. Subsequently, the modified GO was stirred with 2-arm polyetheylene glycol-amine (20 mg) and EDC (3.83 mg·mL^{-1}) for 12 h, and the reaction was terminated by adding mercaptoethanol (5 mL). The final colloidal product was obtained by collecting the supernatant via centrifugation (45,000 rpm) in 2× phosphate-buffered solution (PBS, 20 mL) [14].

2.4 Drug loading

DOX was first dissolved in PBS at pH = 8.0. MLDH nanosheet (0.08605 mg·mL^{-1}) suspensions were mixed with various concentrations of DOX solution (from 0.2 to 1.6 mg·mL^{-1}) followed by stirring at 27 ˚C for 24 h. Afterwards, the as-prepared sample was centrifuged at 5,000 rpm for 10 min to remove the excess DOX. The loading of SN38 by MLDHs was carried out with the same procedure. For the preparation of FA-DOX/MLDHs, DOX (0.8 mg·mL^{-1}) and FA (1.6 mg·mL^{-1}) were simultaneously added into the MLDH suspension (10 mL, 0.08605 mg·mL^{-1}) with stirring at room temperature for 24 h. After centrifugation at 5,000 rpm for 10 min, FA-DOX/MLDHs were obtained and re-dispersed in water.

2.5 *In vitro* studies on tumor cells

KB cells and L-02 cells were incubated in 25 cm^2 cell culture flasks with Dulbecco's modified Eagle's medium consisting of 1% penicillin-streptomycin and 10% fetal bovine serum at 37 ˚C in a 5% CO_2 atmosphere. When the cells reached about 80% confluency, 1.0 mL of 0.25% trypsin was added to detach them from the flask within 5 min at 37 ˚C.

To study the cellular uptake and carry out fluorescence imaging of the drug, KB cells with 100 μL of medium were grown and expanded in 96-well plates at a density of 1 × 10^4 cells/well for 24 h. Pristine DOX, DOX/MLDHs, and FA-DOX/MLDHs (equivalent DOX: 10 μg·mL^{-1}) were added into the wells. After another 3 h of incubation, excess drugs were washed off with PBS four times. Subsequently, the cells were stained by 4',6-diamidino-2-phenylindole (DAPI) for 30 min and washed again with PBS before observation by fluorescence microscopy. Moreover, flow cytometry was used to measure cellular DOX fluorescence intensity and to determine the drug uptake.

To study the integrated performance of DOX, DOX/MLDHs, DOX/GO, FA-DOX/MLDHs, and FA-DOX/GO, KB cells were used to evaluate anticancer activity while L-02 cells were used to evaluate cytotoxicity. Specifically, KB cells and L-02 cells were seeded into 96-well plates with 100 μL of medium at a density of 1 × 10^4 cells/well for 24 h, and then the drug samples were added with DOX concentrations ranging from 1.25 to 20 μg·mL^{-1}. After incubating for another 24 h, 3-(4,5-dimethylthiazol-2-yl)-2,5-diphenyltetrazolium bromide (MTT) was used to detect the cell viability.

In the cellular imaging experiment, KB cells and L-02 cells (1 × 10^4 cells/well) were seeded into two 96-well plates and incubated for 24 h. The cells were treated with 10 μg·mL^{-1} DOX, DOX/MLDHs, and FA-DOX/MLDHs, and then incubated at 37 ˚C for another 24 h. After thoroughly washing with PBS, cells were stained with propidium iodide (PI) and observed using optical microscopy.

2.6 Model construction

The model of DOX adsorbed on the MgAl-LDH monolayer (named DOX/MLDHs) was constructed by putting DOX anions on the MLDH surface. The lattice parameters of DOX/MLDHs were $\alpha = \beta = \gamma = 90°$, a = 45.00 Å, b = 51.96 Å, and c = 28.84 Å. A layer

of MLDHs with a Mg:Al molar ratio of 4 was placed in the middle of the cell. Twenty DOX anions were adsorbed on the surface of the MLDHs. Water molecules were introduced into the cell to simulate the aqueous environment.

The model of DOX solution was constructed by putting DOX in the solvent box with *P*1 symmetry. The lattice parameters of the solvent box were $\alpha = \beta = \gamma = 90°$, $a = b = 50.00$ Å, and $c = 25.00$ Å. Four DOX molecules were introduced into the solvent box. The density of the solution was 1.0 g·cm^{-3}.

2.7 Computational method

All molecular dynamics (MD) simulations were performed by adopting the force field of layered double hydroxide force field (LDHFF) [41] in isothermal-isobaric ensemble, with a temperature of 298 K and a pressure of 0.1 MPa. The temperature and pressure were controlled using the Andersen method [42] and the Berendsen method [43], respectively. The long-range coulombic interactions were computed by the Ewald summation technique [44] and the van der Waals interactions were calculated using a "spline-cutoff" method. The time step was set to be 1 fs. All MD simulations were carried out using the Forcite module in the Materials Studio version 5.5 software package (Accelrys Software Inc., San Diego, CA). For the model of DOX solution, the temperature was raised from 1 to 298 K by a simulated annealing of 10 ps with a constant volume before MD simulations. For both models, MD simulations of 400 ps were performed.

The dynamic trajectories of the last 100 ps were recorded every 1 ps for both models to calculate the diffusion coefficient *D* with the Einstein equation [45]

$$D = \lim_{t\to\infty}(r(0) - r(t))^2 \quad (1)$$

where t is time, $r(t)$ denotes the Cartesian position vector of DOX at the corresponding time t, and the term inside the brackets is the mean squared displacement of DOX. The binding energy (E_B) of DOX in the DOX/MLDHs model was calculated by

$$E_B = E_{model} - (E_{DOX} + E_{model\ without\ DOX}) \quad (2)$$

where E_{model}, E_{DOX}, and $E_{model\ without\ DOX}$ represent the energy of the whole model, DOX, and the model without DOX, respectively.

2.8 Sample characterization

Powder X-ray diffraction (XRD) patterns were collected on a Shimadzu XRD-6000 diffractometer ranging from 3° to 70° (reflection mode, Cu Kα radiation λ = 0.154056 nm at 40 kV with a scan step of 0.04°). High-resolution transmission electron microscope (HRTEM) images were recorded on a JEOL JEM-2100 TEM at an accelerating voltage of 200 kV. Atomic force microscopy (AFM) was performed on a NanoScope IIIa from Veeco Instruments. UV-vis absorption spectra were performed in the range of 200 to 700 nm using a Shimadzu U-3000 spectrophotometer and the slit width was 1.0 nm. Fluorescence spectra were collected on a RF-5301PC fluorospectrophotometer with excitation wavelengths of 480 nm for DOX/MLDHs and 380 nm for SN38/MLDHs. The width of the slit for both excitation and emission was 5 nm. Steady-state polarized photoluminescence measurements were recorded with an Edinburgh Instruments' FLS 980 fluorospectrophotometer. Fourier transform infrared (FT-IR) spectra were recorded at 2 cm^{-1} resolution in the range of 4,000 to 400 cm^{-1} on a Nicolet 605 XB FT-IR spectrometer. Inductively coupled plasma atomic emission spectroscopy (ICP-AES) was used to analyze the metal content of the samples on a Shimadzu ICPS-7500 instrument. Photon correlation spectroscopy was conducted to record Zeta potential and hydrodynamic diameter was measured by dynamic lighting scattering using a Nanosizer Nano ZS from MALVERN instruments. Cell imaging was carried out on a Nikon Ti-s fluorescence microscope and TCS SP5 two-photon confocal microscope (Leica, Germany). Flow cytometry measurement was conducted by MoFlo XDP (Beckman Coulter, Brea, CA, USA).

3 Results and discussion

3.1 Structural and morphological characterization of MLDH nanosheets

MLDH nanosheets were synthesized through a facile method similar to that in previous work [39] with some modifications. The bulk MgAl-LDH colloid

sample showed the (003) diffraction peak at $2\theta = 11.68°$ (Fig. 1(a); black line), but this was not observed for the MLDH colloid sample (Fig, 1(a); red line), implying the lack of long-range ordered structure in the latter sample (the peak at 23.64° is assigned to the polyethylene terephthalate (PET) film substrate). When the above MLDH sample was dried, an intense diffraction peak appeared at 11.29° (Fig. 1(a); blue line), which is ascribed to the re-stacking of the MLDH nanosheets. Figure 1(b) shows the AFM image of one single MLDH nanosheet with a thickness of ~ 0.8 nm, which is close to the value obtained from the formamide delamination method [46], indicating the successful synthesis of MLDH nanosheets. The morphology of MLDH nanosheets was further characterized by HRTEM, from which a uniform hexagonal plate-like particle with a lateral size of ~ 40 nm was observed (Fig. 1(c)). Moreover, the HRTEM image also displays a high dispersion of MLDH nanosheets, which is in agreement with the AFM image. The lattice fringe of 0.178 nm is attributed to the (110) plane of an LDH phase (Fig. 1(c), inset). In addition, the equivalent hydrodynamic diameter of MLDH nanosheets in aqueous solution was measured to be ~ 50 nm (Fig. 1(d)), similar to the size observed by HRTEM.

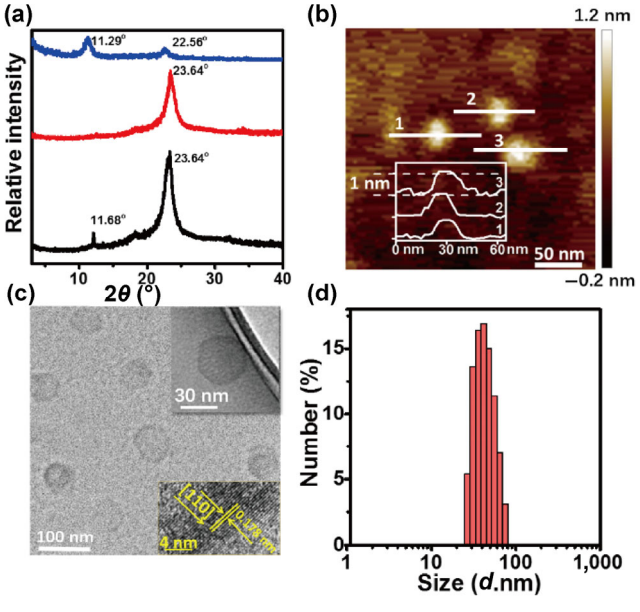

Figure 1 (a) XRD patterns of bulk LDH colloid (black line), MLDH colloid (red line), and the re-stacking of MLDH nanosheets (blue line). (b) AFM image, (c) HRTEM image, and (d) particle size distribution of MLDH nanosheets. The insets in (c) show a high magnification image and crystal lattice.

3.2 Physicochemical property of DOX/MLDHs

We first investigated the loading capacity of the universal chemotherapy drug DOX in the MLDH nanosheets. With the increase in initial DOX concentration, the composite material DOX/MLDHs showed an increasingly enhanced UV-vis absorption peak at 488 nm (characteristic peak of DOX, Fig. 2(a)). The loading capacity of DOX was calculated to be 3.6 mg·mg^{-1} with an initial drug concentration of 1.6 mg·mL^{-1} (Fig. 2(b)), which is significantly larger than those of other reported nanocarriers [36–38]. The fluorescence spectra of DOX/MLDHs also showed a similar tendency: The intensity was gradually enhanced with the increase in initial DOX concentration (Fig. 2(c)). The FT-IR spectra of these DOX/MLDH samples confirmed the loading of DOX by MLDH nanosheets. Compared with MLDHs, the new bands observed at 1,184 and 1,497 cm^{-1} are attributed to the $\delta(CH_3O–)$ stretching and δ(N–H) vibration of DOX (Fig. 2(d)), respectively. Furthermore, the Zeta potential of these DOX/MLDH samples decreased from +25.7 to –3.2 mV (Fig. S1 in the Electronic Supplementary Material (ESM)) with the increase in DOX loading amount. The Mg/Al ratio of these composites was measured by ICP-AES (Table S1 in the ESM), which maintained the initial ratio of MLDH nanosheets. The equivalent

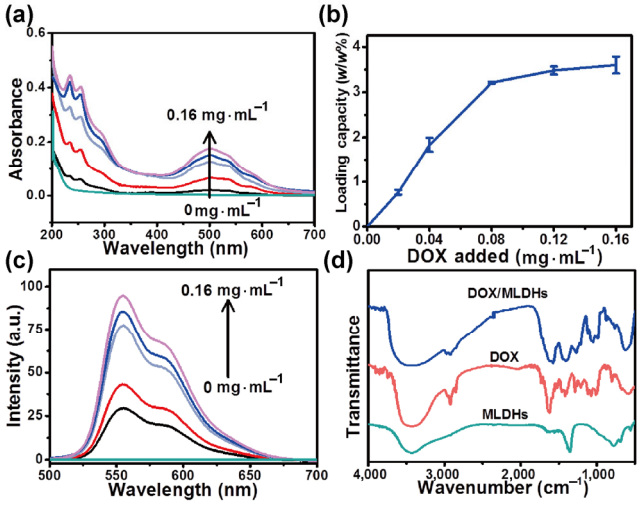

Figure 2 (a) UV-vis absorption spectra, (b) loading capacities, and (c) fluorescence spectra of DOX/MLDH samples with various concentrations of DOX (0, 0.02, 0.04, 0.08, 0.12, and 0.16 mg·mL^{-1}). (d) FT-IR spectra of DOX, MLDHs, and DOX/MLDHs.

hydrodynamic diameter of these DOX/MLDH samples with various loading amounts revealed a very close diameter range (Fig. S2 in the ESM: 60 to 100 nm). In addition, we also evaluated the loading capacity of SN38, another chemotherapy drug, in MLDHs. The UV-vis absorption, photoluminescence (PL), and FT-IR spectrum demonstrated the successful loading of SN38 with a high capacity of 1.4 mg·mg^{-1} (Fig. S3 in the ESM), indicating the universality of MLDH nanosheets as drug carriers.

The intermolecular interaction and configuration between the drug and MLDHs are key factors for drug release and anticancer effect. The interaction between DOX and MLDHs was first studied by isothermal titration calorimetry. As shown in Fig. S4 (in the ESM), the values of ΔH and $-T\Delta S$ are negative, indicating the formation of electrostatic interaction between DOX and MLDHs and the spontaneous loading of DOX onto MLDHs. To further investigate the molecular configuration of DOX on the surface of MLDHs, the luminescence anisotropy was measured with the glancing incidence geometry (Fig. S5 in the ESM).

The in-plane polarized excitation light from parallel and perpendicular directions results in the anisotropy value (r), which increases along with the enhanced order of arranged molecules. The r value of pristine DOX is nearly 0 while that of DOX/MLDHs is calculated to be 0.65, which confirms the ordered alignment of DOX on MLDH nanosheets. Moreover, the configuration of the DOX molecule was further investigated by molecular dynamics (MD) simulations. Figure 3(a) shows the optimized geometry of the DOX/MLDHs model after MD simulations, in which the orientational angle θ of DOX toward MLDHs was calculated to be 10.11° (Fig. S6 in the ESM). First principle was used to calculate the binding energy between DOX and MLDHs (see ESM for details), and the results showed obvious electrostatic interaction (E_B = 15.90 eV per MLDH monomer). To better simulate the drug release behavior in the MLDH system, DOX molecules were set in aqueous solution and on the surface of MLDH nanosheets to record the dynamic trajectory (Figs. 3(b) and 3(c)). The average diffusion coefficients of DOX (based on four DOX molecules; Einstein equation) were calculated to be 5.98 × 10^{-6} and 1.64 × 10^{-6} cm^2·s^{-1} for DOX solution and DOX/MLDHs, respectively (Figs. 3(d) and 3(e)), indicating a depressed diffusion caused by MLDHs through electrostatic interaction.

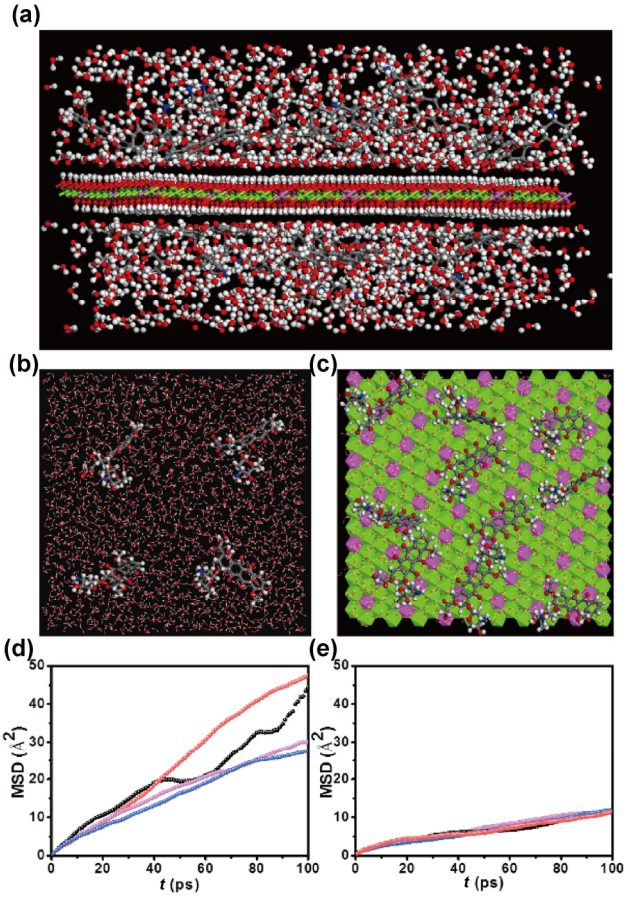

Figure 3 (a) The optimized geometry of DOX/MLDHs model (white H, red O, pink Al, green Mg, gray C, blue N). The optimized geometries model for DOX release: (b) DOX in aqueous solution and (c) DOX on MLDH nanosheets. The mean squared displacement of DOX molecules (d) in aqueous solution and (e) on MLDH nanosheets within 100 ps (each curve represents one DOX molecule).

We then introduced FA to prepare a targeting composite FA-DOX/MLDHs with a nominal DOX/FA ratio of 1:2. The FT-IR spectrum of FA-DOX/MLDHs (Fig. S7 in the ESM) showed characteristic bands at 1,607 and 1,401 cm^{-1}, corresponding to the –C=N of the pterin ring and the symmetrical and asymmetric C=O vibrations of FA, respectively. Moreover, new absorption bands at 290 and 310 nm due to FA were observed accompanying the one at 488 nm ascribed to DOX (Fig. 4(a)). The PL spectra of DOX, DOX/MLDHs, and FA-DOX/MLDHs are displayed in Fig. 4(b). The intensity of two peaks at 550 and 600 nm for pristine DOX was ~ 6 times

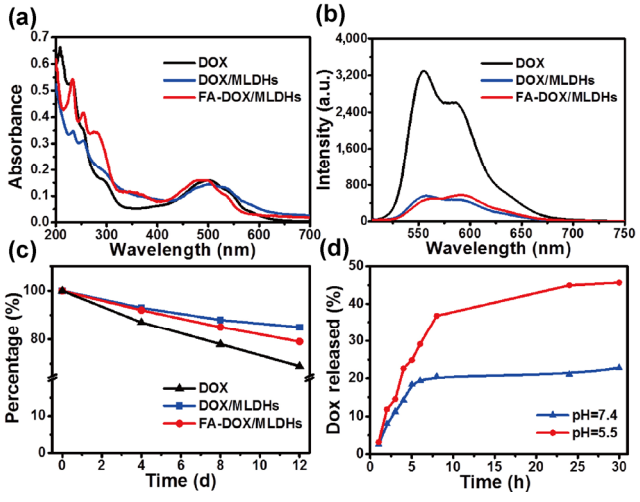

Figure 4 (a) UV-vis absorption spectra, (b) fluorescence spectra, and (c) stability tests of DOX, DOX/MLDHs, and FA-DOX/MLDHs. (d) Cumulative DOX release from FA-DOX/MLDHs under different simulant physiological condition of pH = 7.4 and pH = 5.5.

higher than that of DOX/MLDHs and FA-DOX/MLDHs with an equivalent amount of DOX and was due to the variation in microenvironment.

The morphology of DOX/MLDHs and FA-DOX/MLDHs was further studied by AFM and HRTEM (Fig. 5). The uniform plate-like morphology and the monolayer structure of both DOX/MLDHs and FA-DOX/MLDHs were well maintained with a particle size of ~ 60 nm. However, the thickness of DOX/MLDHs and FA-DOX/MLDHs increased slightly compared with that of pristine MLDHs as a result of the conjunction of DOX and FA. The stability test was performed at 37 ˚C, and UV-vis absorption spectra were recorded at various time points. Pristine DOX showed a sharp decrease from 100% to 69% within 12 days while DOX/MLDHs and FA-DOX/MLDHs showed a gentle drop of 11% and 18% (Fig. 4(c)), respectively. In addition, the release behavior of FA-DOX/MLDHs was investigated (Fig. 4(d)). At pH = 7.4, only 21.1% of the total loaded DOX was released from FA-DOX/MLDHs within 24 h; in contrast, 45.0% of DOX was released after 24 h at pH = 5.5. The enhanced release may have resulted from the ablation of MLDH nanosheets under a weak acidic condition. As shown in Figs. S8(a)–S8(c) in the ESM, the MLDH nanosheets dissolved gradually in solution (pH = 5.5) from 5 to 20 h, with a decrease in the average particle size from 40 to 20 nm (Figs. S8(d)–S8(f) in the ESM). The results demonstrated the ablation of MLDH nanosheets in a weak acidic environment. Hence, it is conducive that selective release of FA-DOX/MLDHs was achieved in cancer cells (pH = 5.5) instead of in normal cells (pH = 7.4), which would result in enhanced anticancer activity and low cytotoxicity to normal cells.

3.3 *In vitro* fluorescence imaging and anticancer performance

Because drug intake is the key point in cancer therapy,

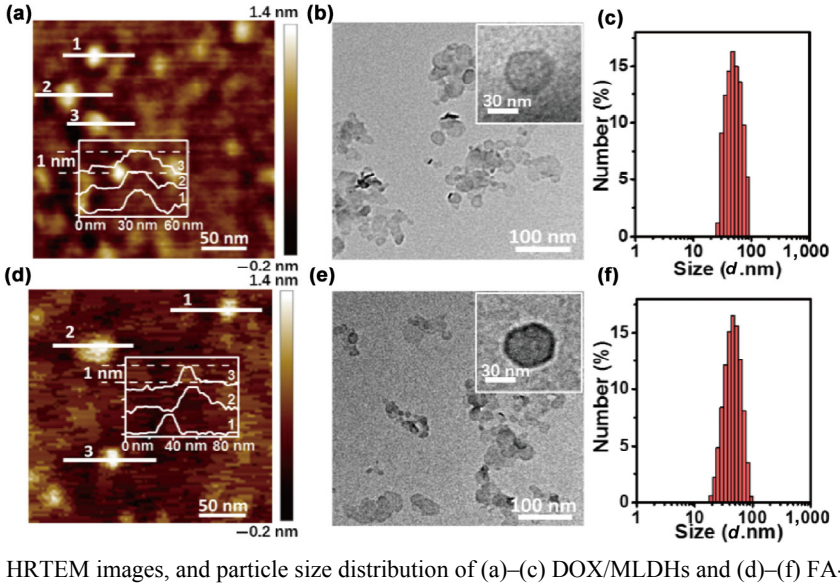

Figure 5 AFM images, HRTEM images, and particle size distribution of (a)–(c) DOX/MLDHs and (d)–(f) FA-DOX/MLDHs.

we investigated the efficiency of cancer cell internalization of the drug by fluorescence imaging. We used graphene oxide (GO) nanosheets to prepare DOX/GO and FA-DOX/GO as control samples, and UV-vis spectra confirmed drug loading (Fig. S9 in the ESM). The drug release profile of FA-DOX/GO was also studied and the result showed pH-responsive release behavior (Fig. S10 in the ESM). KB cells were incubated with DOX, DOX/MLDHs, DOX-FA/MLDHs, DOX/GO, or FA-DOX/GO for 3 h before their fluorescence images were taken. As shown in Fig. 6(a), KB cells incubated with pristine DOX showed strong red fluorescence. For DOX/MLDHs, a relatively weak red signal was detected, indicating a low intake of DOX/MLDHs by KB cells. In contrast, the introduction of FA greatly contributed to the enhancement of the fluorescence intensity of FA-DOX/MLDHs, indicating the better intake performance due to the targeting ability of FA towards KB cells. In addition, a FA-negative cell line (L-02) was used as a negative comparison. As shown in Fig. S11 (in the ESM), the fluorescence intensity of L-02 cells showed no difference between DOX/MLDHs and FA-DOX/MLDHs. However, the fluorescence intensity of KB cells incubated with FA-DOX/MLDHs was significantly higher than that of L-02 cells under the same conditions, further demonstrating a much stronger targeting ability of FA-DOX/MLDHs towards KB cells. Moreover, for the above three samples, the overlapped red signal from DOX and the blue signal from DAPI were detected, manifesting that these samples were located in the cell cytoplasm. The cell intake was further studied by confocal microscopy and the results also indicated that the fluorescence intensity of cancer cells incubated with FA-DOX/MLDHs was stronger than that with DOX/MLDH (Fig. 6(b)). In addition, we used flow cytometry to quantitatively characterize drug intake. As shown in Fig. 6(c), DOX and FA-DOX/MLDHs displayed similar fluorescence signals, much superior to that of DOX/MLDHs. However, both the fluorescence spectra and flow cytometry showed weak fluorescence signals for DOX/GO and FA-DOX/GO samples (Fig. S12 in the ESM), which may have resulted from the fluorescence quenching of DOX by GO (Fig. S13 in the ESM). The anticancer performance of DOX, DOX/MLDHs, FA-DOX/MLDHs, DOX/GO, and FA-DOX/GO was further investigated by *in vitro* tests. The cytotoxicity of the drug carriers (MLDHs or GO) was first evaluated in KB cells and normal liver L-02 cells (Fig. S14 in the ESM). In the presence of MLDHs, the cell viability was maintained at 99.2% and 93.2% for KB cells and L-02 cells (concentration as high as 200 $\mu g \cdot mL^{-1}$), respectively. However, only 51.5% (KB cells) and 59.4% (L-02 cells) cell viability were observed in the presence of GO at the same concentration. The results above indicate a superior biocompatibility of MLDHs to GO.

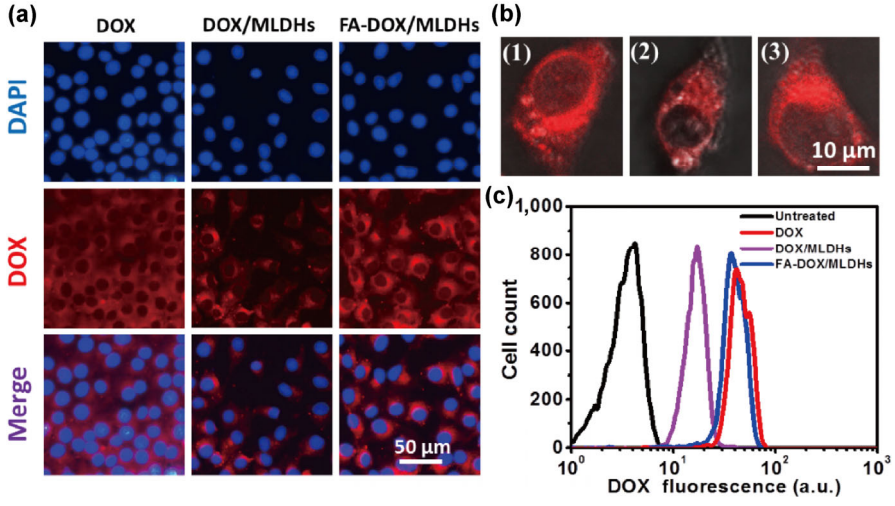

Figure 6 (a) Fluorescence images of KB cells incubated with DOX, DOX/MLDHs, and FA-DOX/MLDHs for 3 h (equivalent DOX: 10 $\mu g \cdot mL^{-1}$). (b) Confocal fluorescence images of KB cells after treatment with various drugs for 3 h (equivalent DOX: 10 $\mu g \cdot mL^{-1}$): (1) DOX, (2) DOX/MLDHs, and (3) FA-DOX/MLDHs. (c) Flow cytometry measurement of cellular fluorescence treated with DOX, DOX/MLDHs, and FA-DOX/MLDHs with the same concentration of DOX (10 $\mu g \cdot mL^{-1}$).

Subsequently, DOX, DOX/MLDHs, FA-DOX/MLDHs, DOX/GO, and FA-DOX/GO were added into KB cells with equivalent DOX concentrations from 1 to 20 μg·mL^{-1}, and the cells were further incubated for 24 h. 3-(4,5-dimethylthiazol-2-yl)-2,5-diphenyltetrazolium bromide (MTT) assay was performed after thoroughly washing with PBS. As shown in Fig. 7(a), a gradually enhanced anticancer effect could be seen as the dosage increased from 1 to 20 μg·mL^{-1}. The half maximal inhibitory concentration (IC_{50}) increased as follows: DOX (3.84 μg·mL^{-1}) < FA-DOX/MLDHs (4.90 μg·mL^{-1}) < DOX/MLDHs (7.68 μg·mL^{-1}) < FA-DOX/GO (10.0 μg·mL^{-1}) < DOX/GO (15.3 μg·mL^{-1}). Pristine DOX showed the lowest value of IC_{50} as the hybrid drugs undergo an uptake-delivery-release procedure while DOX can be absorbed immediately. As drug carriers, MLDHs displayed a systematically lower IC_{50} than GO, which was related to the weak acid microenvironment in cancer cells that facilitates the dissolution of MLDHs and a quick release of DOX. Furthermore, the anticancer efficacy of FA-DOX/MLDHs was remarkably enhanced relative to that of DOX/MLDHs, demonstrating the targeted ability of FA towards KB cells. In addition, the cytotoxicity was investigated for these five samples

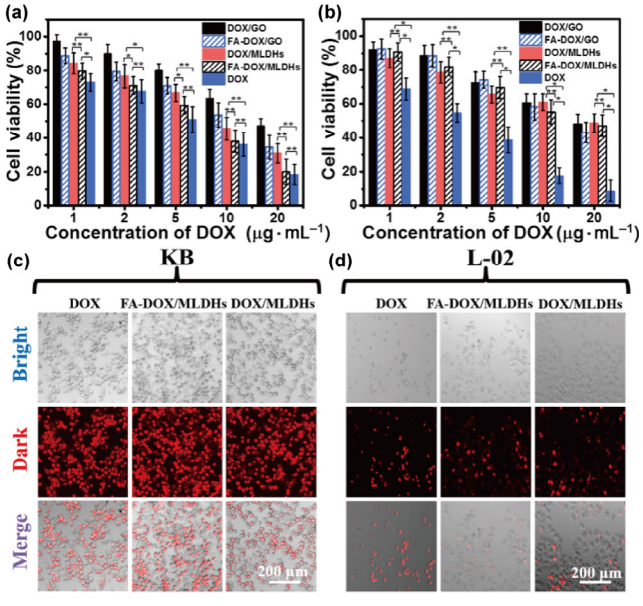

Figure 7 MTT assay of viabilities after incubation with free DOX, DOX/MLDHs, FA-DOX/MLDHs, DOX/GO, and FA-DOX/GO with various concentrations for 24 h: (a) KB cells and (b) L-02 cells. Fluorescence images of (c) KB cells and (d) L-02 cells stained with PI after incubated with DOX, DOX/MLDHs, and FA-DOX/MLDHs (equivalent DOX: 10 μg·mL^{-1}. *p < 0.05, **p < 0.01).

with various drug concentrations toward L-02 cells. As seen in Fig. 7(b), L-02 cells showed excellent tolerance against DOX-FA/MLDHs and FA-DOX/GO with IC_{50} values of 13.84, and 13.85 μg·mL^{-1}, respectively. In contrast, pristine DOX displayed rather strong cytotoxicity toward L-02 cells (IC_{50} = 2.41 μg·mL^{-1}). Therefore, FA-DOX/MLDHs exhibited superior biocompatibility and excellent anticancer activity. To observe the anticancer effect of the drug directly, the dead KB cells were stained with PI. Figure 7(c) shows the apoptosis of KB cells treated by pristine DOX, DOX/MLDHs, and FA-DOX/MLDHs with the same DOX dosage (10 μg·mL^{-1}). As shown in Fig. 7(c), the addition of DOX/MLDHs only showed weak anticancer efficiency as cell apoptosis occurred partially. In contrast, an intense PI signal can be observed in the group of KB cells treated with DOX, revealing a predominant apoptosis. It is interesting that KB cells treated with FA-DOX/MLDHs also displayed a similar PI signal to those treated with pristine DOX. Moreover, the apoptosis of L-02 cells treated by pristine DOX, DOX/MLDHs, and FA-DOX/MLDHs was further investigated (Fig. 7(d)). DOX/MLDHs and FA-DOX/LDHs somewhat induced cell mortality but DOX caused obvious cytotoxicity. Therefore, although the anticancer performances of FA-DOX/MLDHs and pristine DOX were almost at the same level, the former showed a largely enhanced biocompatibility with weak cytotoxicity toward normal cells as a result of the incorporation of MLDHs as a drug carrier.

4 Conclusions

In summary, we developed 2D MLDH nanosheets with a high specific surface area and abundant combinative sites, which showed an extremely large loading capacity and controllable release of the chemotherapeutic agent DOX. XRD, AFM, and HRTEM confirmed a diameter of 50 nm and a thickness of 0.8 nm for MLDH nanosheets. After further incorporation of FA, the as-synthesized FA-DOX/MLDH composite exhibited good fluorescence imaging, selective anticancer performance, and rather low cytotoxicity to normal cells. In addition, the FA-DOX/MLDH composite displayed high storage stability, good biocompatibility,

and targeting capability. Therefore, this work demonstrates a successful paradigm of a new 2D ultrathin drug carrier via a facile preparation process, which serves as a promising candidate in bioimaging and cancer therapy.

Acknowledgements

This work was supported by National Natural Science Foundation of China (NSFC) (Nos. 21671013 and 21601010), the National Basic Research Program of China (973 Program) (No. 2014CB932103), the Fundamental Research Funds for the Central Universities (Nos. YS 1406, ZY1628, and buctrc201611) and Beijing Natural Science Foundation (No. 2174082).

Electronic Supplementary Material: Supplementary material (TEM, zeta potential, size distribution, UV-vis absorption spectra, fluorescence emission spectra, isothermal titration calorimetry measurements, polarized fluorescence spectra and *in vitro* fluorescence imaging) is available in the online version of this article at https://doi.org/10.1007/s12274-017-1619-y.

References

[1] Song, F.; Hu, X. L. Ultrathin cobalt–manganese layered double hydroxide is an efficient oxygen evolution catalyst. *J. Am. Chem. Soc*. **2014**, *136*, 16481–16484.

[2] Sun, Y. F.; Cheng, H.; Gao, S.; Liu, Q. H.; Sun, Z. H.; Xiao, C.; Wu, C. Z.; Wei, S. Q.; Xie, Y. Atomically thick bismuth selenide freestanding single layers achieving enhanced thermoelectric energy harvesting. *J. Am. Chem. Soc*. **2012**, *134*, 20294–20297.

[3] Wang, K. P.; Wang, J.; Fan, J. T.; Lotya, M.; O'Neill, A.; Fox, D.; Feng, Y. Y.; Zhang, X. Y.; Jiang, B. X.; Zhao, Q. Z. et al. Ultrafast saturable absorption of two-dimensional MoS_2 nanosheets. *ACS Nano* **2013**, *7*, 9260–9267.

[4] Li, X. H.; Zhu, J. M.; Wei, B. Q. Hybrid nanostructures of metal/two-dimensional nanomaterials for plasmon-enhanced applications. *Chem. Soc. Rev*. **2016**, *45*, 3145–3187.

[5] Peng, X.; Peng, L. L.; Wu, C. Z.; Xie, Y. Two dimensional nanomaterials for flexible supercapacitors. *Chem. Soc. Rev*. **2014**, *43*, 3303–3323.

[6] Tan, C. L.; Liu, Z. D.; Huang, W.; Zhang, H. Non-volatile resistive memory devices based on solution-processed ultrathin two-dimensional nanomaterials. *Chem. Soc. Rev*. **2015**, *44*, 2615–2628.

[7] Wang, Y. L.; Cong, C. X.; Yang, W. H.; Shang, J. Z; Peimyoo, N.; Chen, Y.; Kang, J. Y.; Wang, J. P.; Huang, W.; Yu, T. Strain-induced direct–indirect bandgap transition and phonon modulation in monolayer WS_2. *Nano Res*. **2015**, *8*, 2562–2572.

[8] Chimene, D.; Alge, D. L.; Gaharwar, A. K. Two-dimensional nanomaterials for biomedical applications: Emerging trends and future prospects. *Adv. Mater*. **2015**, *27*, 7261–7284.

[9] Lu, X.; Luo, X.; Zhang, J.; Quek, S. Y.; Xiong, Q. H. Lattice vibrations and Raman scattering in two-dimensional layered materials beyond graphene. *Nano Res*. **2016**, *9*, 3559–3597.

[10] Tan, C. L.; Yu, P.; Hu, Y. L.; Chen, J. Z.; Huang, Y.; Cai, Y. Q.; Luo, Z. M.; Li, B.; Lu, Q. P.; Wang, L. H. et al. High-yield exfoliation of ultrathin two-dimensional ternary chalcogenide nanosheets for highly sensitive and selective fluorescence DNA sensors. *J. Am. Chem. Soc*. **2015**, *137*, 10430–10436.

[11] Wang, Z. Y.; Zhu, W. P.; Qiu, Y.; Yi, X.; von dem Bussche, A.; Kane, A.; Gao, H. J.; Koski, K.; Hurt, R. Biological and environmental interactions of emerging two-dimensional nanomaterials. *Chem. Soc. Rev*. **2016**, *45*, 1750–1780.

[12] Chen, Y.; Ye, D. L.; Wu, M. Y.; Chen, H. R.; Zhang, L. L.; Shi, J. L.; Wang, L. Z. Break-up of two-dimensional MnO_2 nanosheets promotes ultrasensitive pH-triggered theranostics of cancer. *Adv. Mater*. **2014**, *26*, 7019–7026.

[13] Feng, L. Y.; Wu, L.; Qu, X. G. New horizons for diagnostics and therapeutic applications of graphene and graphene oxide. *Adv. Mater*. **2013**, *25*, 168–186.

[14] Liu, Z.; Robinson, J. T.; Sun, X. M.; Dai, H. J. PEGylated nanographene oxide for delivery of water-insoluble cancer drugs. *J. Am. Chem. Soc*. **2008**, *130*, 10876–10877.

[15] Liu, T.; Wang, C.; Gu, X.; Gong, H.; Cheng, L.; Shi, X. Z.; Feng, L. Z.; Sun, B. Q.; Liu, Z. Drug delivery with PEGylated MoS_2 nano-sheets for combined photothermal and chemotherapy of cancer. *Adv. Mater*. **2014**, *26*, 3433–3440.

[16] Wang, H.; Yang, X. Z.; Shao, W.; Chen, S. C.; Xie, J. F.; Zhang, X. D.; Wang, J.; Xie, Y. Ultrathin black phosphorus nanosheets for efficient singlet oxygen generation. *J. Am. Chem. Soc*. **2015**, *137*, 11376–11382.

[17] Geim, A.K. Graphene: Status and prospects. *Science* **2009**, *324*, 1530–1538.

[18] Novoselov, K. S.; Geim, A. K.; Morozov, S. V.; Jiang, D.; Zhang, Y.; Dubonos, S. V.; Grigorieva, I. V.; Firsov, A. A. Electric field effect in atomically thin carbon films. *Science* **2004**, *306*, 666–669.

[19] Cheng, L.; Liu, J. J.; Gu, X.; Gong, H.; Shi, X. Z.; Liu, T.; Wang, C.; Wang, X. Y.; Liu, G.; Xing, H. Y. et al. PEGylated WS_2 nanosheets as a multifunctional theranostic agent for *in vivo* dual-modal CT/photoacoustic imaging guided photothermal therapy. *Adv. Mate*r. **2014**, *26*, 1886–1893.

[20] Feng, L. Y.; Li, W.; Ren, J. S.; Qu, X. G.Electrochemically

and DNA-triggered cell release from ferrocene/β-cyclodextrin and aptamer modified dualfunctionalized graphene substrate. *Nano Res.* **2015**, *8*, 887–899.

[21] Li, M.; Zhao, A. D.; Dong, K.; Li, W.; Ren, J. S.; Qu, X. G. Chemically exfoliated WS_2 nanosheets efficiently inhibit amyloid β-peptide aggregation and can be used for photothermal treatment of Alzheimer's disease. *Nano Res.* **2015**, *8*, 3216–3227.

[22] Wang, Q.; Tay, H. H.; Zhong, Z. Y.; Luo, J. Z.; Borgna, A. Synthesis of high-temperature CO_2 adsorbents from organo-layered double hydroxides with markedly improved CO_2 capture capacity. *EnergyEnviron. Sci.* **2012**, *5*, 7526–7530.

[23] Qiao, Y. Q.; Wang, J. Y.; Huang, L.; Zheng, Q. W.; O'Hare, D.; Wang, Q. LDH/$MgCO_3$ hybrid multilayer on an aluminium substrate as a novel high-temperature CO_2 adsorbent. *RSC Adv*. **2015**, *5*, 82777–82780.

[24] Williams, G. R.; Fogg, A. M.;Sloan, J.; Taviot-Guého, C.; O'Hare, D. Staging during anion-exchange intercalation into $[LiAl_2(OH)_6]Cl{\cdot}yH_2O$: Structural and mechanistic insights. *Dalton Trans.* **2007**, 3499–3506.

[25] Varadwaj, G. B. B.; Nyamori, V. O. Layered double hydroxide- and graphene-based hierarchical nanocomposites: Synthetic strategies and promising applications in energy conversion and conservation. *Nano Res.* **2016**, *9*, 3598–3621.

[26] Evans, D. G.; Duan, X. Preparation of layered double hydroxides and their applications as additives in polymers, as precursors to magnetic materials and in biology and medicine. *Chem. Commun*. **2006**, 485–496.

[27] Li, L.; Gu, W. Y.; Liu, J.; Yan, S. Y.; Xu, Z. P. Amine-functionalized SiO_2 nanodot-coated layered double hydroxide nanocomposites for enhanced gene delivery. *Nano Res.* **2015**, *8*, 682–694.

[28] Liu, Z. L.; Tian, D. Y.; Li, S. P.; Li, X. D.; Lu, T. H. MTX/LDHs hybrids synthesized from reverse microemulsions: Particle control and bioassay study. *Int. J. Pharm*. **2014**, *473*, 414–425.

[29] Li, L.; Gu, W. Y.; Chen, J. Z.; Chen, W. Y.; Xu, Z. P. Co-delivery of siRNAs and anti-cancer drugs using layered double hydroxide nanoparticles. *Biomaterials* **2014**, *35*, 3331–3339.

[30] Park, D. H.; Kim, J. E.; Oh, J. M.; Shul, Y. G.; Choy, J. H. DNA core@inorganic shell. *J. Am. Chem. Soc*. **2010**, *132*, 16735–16736.

[31] Liang, R. Z.; Tian, R.; Ma, L. N.; Zhang, L. L.; Hu, Y. L.; Wang, J.; Wei, M.; Yan, D.; Evans, D. G.; Duan, X. A supermolecular photosensitizer with excellent anticancer performance in photodynamic therapy. *Adv. Funct. Mater*. **2014**, *24*, 3144–3151.

[32] Song, F.; Hu, X. L. Exfoliation of layered double hydroxides for enhanced oxygen evolution catalysis. *Nat. Commun*. **2014**, *5*, 4477.

[33] Wang, Q.; Tang, S. V. Y.; Lester, E.; O'Hare, D. Synthesis of ultrafine layered double hydroxide (LDHs) nanoplates using a continuous-flow hydrothermal reactor. *Nanoscale* **2013**, *5*, 114–117.

[34] Yan, Y. X.; Liu, Q.; Wang, J.; Wei, J. B.; Gao, Z.; Mann, T.; Li, Z. S.; He, Y.; Zhang, M.; Liu, L. H. Single-step synthesis of layered double hydroxides ultrathin nanosheets. *J. Colloid Interface Sci*. **2012**, *371*, 15–19.

[35] Yan, D. P.; Lu, J.; Ma, J.; Wei, M.; Evans, D. G.; Duan, X. Reversibly thermochromic, fluorescent ultrathin films with a supramolecular architecture. *Angew. Chem., Int. Ed*. **2011**, *50*, 720–723.

[36] Zhang, L. M.; Xia, J. G.; Zhao, Q. H.; Liu, L. W.; Zhang, Z. J. Functional graphene oxide as a nanocarrier for controlled loading and targeted delivery of mixed anticancer drugs. *Small* **2010**, *6*, 537–544.

[37] Zhang, Z. J.; Wang, J.; Nie, X.; Wen, T.; Ji, Y. L.; Wu, X. C.; Zhao, Y. L.; Chen, C. Y. Near infrared laser-induced targeted cancer therapy using thermoresponsive polymer encapsulated gold nanorods. *J. Am. Chem. Soc*. **2014**, *136*, 7317–7326.

[38] Tian, Y. H.; Li, S. P.; Song, J.; Ji, T. J.; Zhu, M. T.; Anderson, G. J.; Wei, J. Y.; Nie, G. J. A doxorubicin delivery platform using engineered natural membrane vesicle exosomes for targeted tumor therapy. *Biomaterials* **2014**, *35*, 2383–2390.

[39] Yu, J. F.; Martin, B. R.; Clearfield, A.; Luo, Z. P.; Sun, L. Y. One-step direct synthesis of layered double hydroxide single-layer nanosheets. *Nanoscale* **2015**, *7*, 9448–9451.

[40] Liu, Z.; Sun, X. M.; Nakayama-Ratchford, N.; Dai, H. J. Supramolecular chemistry on water-soluble carbon nanotubes for drug loading and delivery. *ACS Nano* **2007**, *1*, 50–56.

[41] Zhang, S. T; Yan, H.; Wei, M.; Evans, D. G.; Duan, X. Valence force field for layered double hydroxide materials based on the parameterization of octahedrally coordinated metal cations. *J. Phys. Chem. C***2012**, *116*, 3421–3431.

[42] Andersen, H. C. Molecular dynamics simulations at constant pressure and/or temperature. *J. Chem. Phys.* **1980**, *72*, 2384–2393.

[43] Berendsen, H. J. C.; Postma, J. P. M.; Van Gunsteren, W. F.; DiNola, A.; Haak, J. R. Molecular dynamics with coupling to an external bath. *J. Chem. Phys.* **1984**, *81*, 3684–3690.

[44] Allen, M. P.; Tildesley, D. J. *Computer Simulation of Liquids;* Clarendon Press:Oxford, U. K., 1987.

[45] Frenkel, D.; Smit, B. *Understanding Molecular Simulation: From Algorithms to Applications;* 2nd ed., Academic Press: San Diego, 2002.

[46] Liang, R. Z.; Xu, S. M.; Yan, D. P.; Shi, W. Y.; Tian, R.; Yan, H.; Wei, M.; Evans, D. G.; Duan, X. CdTe quantum dots/layered double hydroxide ultrathin films with multicolor light emission via layer-by-layer assembly. *Adv. Funct. Mater.* **2012**, *22*, 4940–4948.